Topological Summaries of Tumor Images Improve Prediction of Disease Free Survival in Glioblastoma Multiforme

Lorin Crawford[1], Anthea Monod[2,*], Andrew X. Chen[2], Sayan Mukherjee[1,3], and Raúl Rabadán[2,4]

1 Department of Statistical Science, Duke University, Durham, NC 27708, USA
2 Department of Biomedical Informatics, Columbia University, NY, NY 10032, USA
3 Departments of Computer Science, Mathematics, and Biostatistics & Bioinformatics, Duke University, Durham, NC, 27708, USA
4 Departments of Systems Biology, Columbia University, NY, NY 10032, USA

*Corresponding Email: am4691@cumc.columbia.edu

arXiv:1611.06818v1 [stat.AP] 21 Nov 2016

Abstract

In this paper we propose a novel statistic, the smooth Euler characteristic transform (SECT). The SECT is designed to integrate shape information into standard statistical models. More specifically, the SECT allows us to represent shapes as a collection of vectors with little to no loss in information. As a result, detailed shape information can be combined with biomarkers such as gene expression in standard statistical frameworks, such as linear mixed models. We illustrate the utility of the SECT in radiogenomics by predicting disease free survival in glioblastoma multiforme patients based on the shape of their tumor as assayed by magnetic resonance imaging. We show that the SECT features outperform gene expression, volumetric features, and morphometric features in predicting disease free survival.

Keywords: Topological Data Analysis, Euler Characteristic Transform, Glioblastoma Multiforme, Radiogenomics

1 Introduction

Radiogenomics, or imaging genomics, focuses on understanding the relationship between clinical imaging and functional genomic variation. In cancer applications, radiogenomic analyses often involve integrating magnetic resonance imaging (MRI) data, gene expression data, and gene mutation status in order to make more informed clinical decisions or to better understand the etiology of a particular disease. This paper makes two contributions to the field of radiogenomics. The first contribution is the development of a novel statistic, the smooth Euler characteristic transform (SECT), which is designed to integrate shape information into standard statistical models. The second contribution is a detailed radiogenomic analysis of glioblastoma multiforme with the objective of predicting clinical outcomes using imaging and gene expression data.

Gliomas are a collection of tumors arising from glia or their precursors within the central nervous system. Of all gliomas, glioblastoma multiforme (GBM) is the most aggressive and most common in humans (Holland, 2000). The prognosis for patients with GBM is poor with typical post-diagnosis survival of 12-15 months and the probability of 5 year survival is less than 10% (Patel et al., 2014). In addition, obtaining molecular assays of a tumor from patients with GBM often requires invasive surgical procedures such as stereotactic biopsy or craniotomy. Imaging technologies provide a useful alternative to standard genomic biomarkers, and can help with both the earlier detection and monitoring of tumors.

Imaging technologies have recently been used in cancer research to correlate features from images to clinical outcomes (*e.g.* survival) and molecular biomarkers. One noteworthy effort where

imaging and genomic data have been collected is the Repository of Molecular Brain Neoplasia Data (REMBRANDT) (Clark et al., 2013). Based on the REMBRANDT data, a set of MRI features have been derived in the Visually Accessible Rembrandt Images (VASARI) project. Using the VASARI image features Gutman et al. (2013) and Mazurowski et al. (2013) were able to show that the inclusion of geometric information can improve predictions of survival outcomes. Gevaert et al. (2014) and Macyszyn et al. (2016) expanded on this work by showing that geometric features can also be used to predict specific GBM subtypes. Generating the VASARI features involved annotation by neuroradiologists which is costly and has since motivated the development of fully automated pipelines for GBM image analysis to link the geometry of tumors to patient prognostics (Mazurowski et al., 2014; Rios Velazquez et al., 2015). In Itakura et al. (2015), cancer subtypes defined by imaging features were found to correlate with both survival and the activation of molecular signaling pathways. Typically, the geometric features extracted from images in radiogenomic applications have been limited to gross spatial features such as the presence of multifocal tumors (Liu et al., 2015) or the location of recurrent lesions (Kim et al., 2015).

In this paper, we alternatively explore the use of the SECT as an automated procedure to extract geometric or topological statistics from tumor images. The argument for using the SECT for radiogenomics is that more precise geometric information is captured in robust ways when using topological summaries of a shape. The SECT is a variation of the persistent homology transform (PHT), which was initially introduced by Turner et al. (2014) to represent shapes and measure distances between CT scans of primate bones as an application in geometric morphometrics. The advantage of the SECT over the PHT is that the statistical summary computed by the SECT is a collection of smooth vectors, while the summary generated by the PHT is a collection of persistent homology diagrams (Edelsbrunner et al., 2000) and thus has a complicated representation and geometry (Turner et al., 2014). Therefore, unlike the SECT, the PHT is difficult to incorporate into standard statistical models such a linear mixed models. In this work, we examine in detail how SECT features applied to tumor images from The Cancer Genome Atlas (TCGA) compare to gene expression data, as well as classical volumetric and morphometric features, in predicting two clinical outcomes: disease free survival (DFS) and overall survival (OS). We show that the SECT features outperform gene expression, volumetric features, and morphometric features in predicting DFS.

The remainder of this paper is organized as follows. In Section 2, we describe the SECT in detail and provide a brief description of topological data analysis (TDA). In Section 3, we specify a Bayesian framework that allows us to integrate SECT features with other covariates in an efficient and robust linear mixed model. In Section 4, we use the linear mixed model to compare the utility of the SECT summaries, gene expression data, volumetric features, and morphometric features in predicting survival of patients with GBM. Lastly, we close the paper with a discussion of future directions, limitations of our proposed approach, and some immediate challenges in radiogenomics.

2 Quantifying Tumor Images Using Topological Summaries

In this section, we provide an overview of existing statistical methods for summarizing shapes, and define the smooth Euler characteristic transform (SECT) — a summary statistic that captures the geometry and topology of a shape. We also outline why this statistic is well-suited to integrate shape information into standard statistical models.

2.1 Integral Geometry and Shape Statistics

Classical shape statistics represented three-dimensional shapes as landmark points placed on the shape (Kendall, 1984; Bookstein, 1997; Dryden and Mardia, 1998). This representation was partly due to the limited imaging and processing technology of the time. Raw data themselves were typically collected only as points, or distances between points; and moreover, statistical and computational methodology to be able to model shapes as three-dimensional images simply did not exist. At present, current imaging technologies allow three-dimensional shapes to be represented as meshes — a collection of vertices, faces, and edges. An example of a mesh is depicted in Figure 1(a).

Given the advancement in both imaging technology and computational tools to process the imaging data, classical landmark-based approaches that previously required user-specification of landmarks have become less relevant. Methods have since been developed that generate automated geometric morphometrics, bypassing the need for user-specified landmarks for mesh representations (Boyer et al., 2011; Al-Aifari et al., 2013; Lipman and Daubechies, 2011; Boyer et al., 2015; Gao et al., 2016; Gao et al., 2016). Figure 1(b) illustrates a landmark representation of a molar, to illustrate and compare the difference between mesh and landmark representations of shapes. Note that both user-specified and automated landmark-based methods for geometric morphometrics are known to suffer from structural errors when comparing shapes that are highly dissimilar (Gao et al., 2016; Gao, 2015).

An approach that comprehensively addresses these issues by bypassing both user and automated specification of landmarks, as well as highly dissimilar and non-isomorphic shapes, was developed in Turner et al. (2014) where a statistical summary of the data known as the persistent homology transform (PHT) was used to represent shape. The PHT is a collection of persistence diagrams — multiscale topological summaries used extensively in topological data analysis (TDA).

2.2 Topological Data Analysis: Geometric and Topological Preliminaries

The mesh representation of a shape is an example of a mathematical object known as a simplicial complex, which are important objects of study in TDA. TDA provides a rich array of powerful tools and methodologies built upon a solid foundation of classic mathematical and statistical theory that successfully recovers information and structure of an underlying data space.

A *k-simplex* is the convex hull of $k+1$ affine independent points $v_0, v_1, \dots v_k$, and is denoted by $\sigma = [v_0, v_1, \dots, v_k]$. Examples of k-simplices are points, lines, and triangles. The 0-simplex $[v_0]$ is the vertex v_0, the 1-simplex $[v_0, v_1]$ is the edge between the vertices v_0 and v_1, and the 2-simplex $[v_0, v_1, v_2]$ is the triangle bordered by the edges $[v_0, v_1]$, $[v_1, v_2]$ and $[v_0, v_2]$.

Definition 2.2.1. A *simplicial complex* K is a countable set of simplices such that:

1. Every face of a simplex in K is also in K;
2. If two k-simplices σ_1, σ_2 are in K, then their intersection is either empty or a face of both σ_1 and σ_2.

Homology and Persistence. The PHT statistic was proposed by Turner et al. (2014) as a way of representing shapes, and relies on persistent homology for its calculation. Persistent homology is a mathematical concept of fundamental interest in applied topology, and especially in TDA. In particular, persistent homology is a multi-scale instantiation of the classical concept of homology which we now describe informally. For a more rigorous treatment, see Hatcher (2002) and Munkres (1984).

Given a shape M with a finite simplicial complex representation (mesh) K, a *simplicial k-chain* is a formal linear combination (over $\mathbf{Z}_2$ in this paper) of k-simplices in K. The set of k-chains forms a vector space $C_k(K)$. The *boundary map* is $\partial_k : C_k(K) \to C_{k-1}(K)$, given by

$$\partial_k \left([v_0, v_1, \ldots, v_k]\right) = \sum_{j=0}^{k} [v_0, \ldots, v_{-j}, \ldots, v_k]$$

with linear extension, where v_{-j} denotes that we drop element j. Elements of $B_k(K) = \operatorname{im} \partial_{k+1}$ are called *boundaries*, and elements of $Z_k(K) = \ker \partial_k$ are called *cycles*.

Definition 2.2.2. The k^{th} *homology group* of M is defined by the quotient group

$$H_k(K) := Z_k(K)/B_k(K).$$

The intuition behind a homology group is that it contains information about the structure of K. The zeroth homology group $H_0(X)$ is generated by elements that represent connected components of X. For example, if X has three connected components, then $H_0(X) \cong \mathbf{Z}_2 \oplus \mathbf{Z}_2 \oplus \mathbf{Z}_2$, where $\cong$ denotes group isomorphism. For $k \geq 1$, the k-th homology group $H_k(X)$ is generated by elements representing k-dimensional "holes" or "loops" in X. A k-dimensional hole can be thought of as the result of taking the boundary of a $(k+1)$-dimensional body. The ranks of the homology groups (*i.e.* the number of generators) are called the Betti numbers, and are denoted by $\beta_k(X) := \operatorname{rank}\big(H_k(X)\big)$. The notation $H_*(X)$ refers to all the homology groups simultaneously. In Figure 2, we display the homology of a torus constructed from a simplicial complex.

A filtration $\mathcal{K}$ of simpicial complexes is a family of spaces $\mathcal{K} = \{K_t\}_{t=a}^{b}$ such that $K_{t_1} \subseteq K_{t_2}$ if $t_1 < t_2$. As the parameter t increases, the homology of the spaces K_t may change (*e.g.* components are added and merged, cycles are formed and filled up). The *persistent homology* of $\mathcal{K}$ is denoted by $\mathrm{PH}_*(\mathcal{K})$ and keeps track of the progression of homology groups generated by the filtration. More specifically, the persistent homology contains the information about the homology of the individual spaces $\{K_t\}$, as well as the mappings between the homology of K_{t_1} and K_{t_2} for every $t_1 < t_2$. Note that persistent homology is also equivalently referred to as *persistence*.

The above description of persistent homology is based on simplicial complexes, which are the object of our particular interest since mesh representations of shapes are simplicial complexes. However, we note that persistent homology is a notion that also lends itself to other structures and modes of learning an underlying space from which data is sampled. Another example is the union of balls around the sampled points. We can study the persistence on either of these two structures, since the Nerve Lemma — a powerful result due to Borsuk (1948) — provides homotopy equivalence between simplicial complexes and unions of balls.

Intuitively, the main idea behind persistent homology is to study homology across multiple scales. Rather than restricting ourselves to only one instance of a space, in persistent homology we study the evolution of the topological structure over a filtration of the space, which amounts to beginning with a rigid proximity rule connecting observed data points, and then continuously relaxing this rule — all while studying the corresponding topological progression. Figure 3(a) illustrates five instances of this idea, where the underlying space is an annulus from which points are sampled. Balls are formed around these data points, with radii growing from r_1 through to r_5. We see the homology being captured changes with radius size, which in this case is the proximity rule.

Barcodes and Persistence Diagrams. The persistence of the data is encoded in objects that are parameterizations of these homology groups known as *barcodes*: collections of intervals which

correspond to the lifetimes of topological features. The left endpoint of a bar is the *birth time* of an element in $\mathrm{PH}_*(\mathcal{K})$ and can be thought of as the value of t where this element appears for the first time. Conversely, the right endpoint of a bar is the *death time* and represents the value of t where an element vanishes, or merges with another existing element.

Figure 3 provides an example of a barcode and illustrates the idea behind persistent homology. First, $n = 50$ samples $P_1, \ldots, P_n \in \mathbf{R}^2$ were sampled from a uniform distribution on an annulus, and $X_r = \bigcup_i B_r(P_i)$ is defined to be the union of closed balls around the samples. Increasing r causes X_r to grow. As this happens, connected components merge, cycles are formed and then are filled up. The barcode in Figure 3(b) captures a summary of all the homology features in this process. Specifically, in this image there are two bars that are significantly longer than the others (one in H_0 and one in H_1), indicating that the underlying space has a single connected component and a single cycle, similar to that of the annulus.

Barcodes can therefore be considered as summary statistics of the data generating process, as they sufficiently allow for a reduction in dimension of the ambient space. This information can alternatively be represented by a *persistence diagram*, which takes the birth and death times of each bar in a barcode as an ordered pair (x, y) and produces a scatterplot, thus providing a multi-scale topological summary of the data space. In a persistence diagram, the points lie in $\mathbf{R}^2$ and all the points on the diagonal $x = y$ have infinite multiplicity. The diagonal is included for technical reasons and involves defining a metric on the space of diagrams or barcodes. Points on the diagonal may be intuitively thought of as topological noise, since they are points that are born and die immediately.

Since summary statistics are direct parallels to the invariants of a topological space, considering such topological approaches in data analytics is a way of reducing dimensionality in high-dimensional statistical problems (*i.e.* where the number of covariates is far greater than the number of observations). For a complete discussion on frequently used methodologies in TDA and applied topology, we refer the interested reader to the following works: Carlsson (2009), Carlsson (2014), Edelsbrunner et al. (2000), Ghrist (2008).

2.3 Topological Shape Measures

The SECT is a variation of the PHT due to Turner et al. (2013) and Turner et al. (2014). In this subsection, we will introduce and define the SECT, state some of its properties, and motivate why we propose the SECT be used over the PHT.

The Persistent Homology Transform. Let M be a closed, compact subset (shape) of $\mathbf{R}^d$ that can be written as a finite simplicial complex K. For any unit vector over the unit sphere $\nu \in S^{d-1}$, we define a filtration $K(\nu)$ of K parameterized by a height r as

$$K(\nu)_r = \{x \in K : x \cdot \nu \leq r\} \tag{1}$$

for a unit vector $\nu \in S^{d-1}$. The parameter height function $r_\nu(x)$ is then defined as

$$\begin{aligned} r : \mathbf{R}^2 &\to \mathbf{R} \\ \{x, \nu\} &\mapsto x \cdot \nu \end{aligned} \tag{2}$$

for the same fixed unit $\nu \in S^{d-1}$. See Figure 4 for an example of filtration by a height function. The k-th dimensional persistence diagram $X_k(K, \nu)$ summarizes how the topology of the filtration $K(\nu)$ changes over the height parameter r, as described in the previous subsection.

Definition 2.3.1 (Turner et al. (2014))**.** The *persistent homology transform (PHT)* of $K \subset \mathbf{R}^d$ is the function

$$\begin{aligned} \mathrm{PHT}(K) : S^{d-1} &\to \mathcal{D}^d \\ \nu &\mapsto \big(X_0(K,\nu), X_1(K,\nu), \ldots, X_{d-1}(K,\nu)\big). \end{aligned}$$

The PHT measures the change in homology by the height filtration over all directions on the unit sphere. There are two reasons why the PHT is useful. To illustrate the first, denote the space of persistence diagrams as $\mathcal{D}$ (Mileyko et al., 2011; Turner et al., 2014; Bubenik, 2015), and given two diagrams $X, Y \in \mathcal{D}$, note that the *Wasserstein distance* between the diagrams X and Y is given by

$$\mathrm{dist}(X,Y) = \left(\inf_{\varphi: X \to Y} \sum_{x \in X} \|x - \varphi(x)\| \right),$$

where φ is a bijection between points in X and Y. Let $\mathcal{M}_d$ be the space of subsets of $\mathbf{R}^d$ that can be represented as finite simplicial complexes. The PHT can be used to define a distance metric between shapes or surfaces

$$\mathrm{dist}^{\mathrm{PHT}}_{\mathcal{M}_d}(K_1, K_2) := \sum_{k=0}^{d} \int_{S^{d-1}} \mathrm{dist}\big(X_k(K_1,\nu), X_k(K_2,\nu)\big) d\nu,$$

which allows for comparisons and similarity studies between shapes. Secondly, the PHT preserves information, and a notion of statistical sufficiency was proven for the PHT. Specifically, it was proven in Turner et al. (2014) that the PHT is injective when the domain is $\mathcal{M}_d$ for $d = 2, 3$. In practice, the PHT is not computed using all directions on the sphere. A corresponding proof of stability of the PHT justifies the use of finitely many directions, and gives a corresponding bound on the approximation error.

While the PHT was useful in computing distances between shapes, it is challenging to use in standard likelihood based models. Most widely used likelihood models have an inner product structure between the model parameters and sufficient statistics. The PHT does not admit a simple inner product structure as it is a collection of persistence diagrams, and the geometry of the space of persistence diagrams is known to be an Alexandrov space with curvature bounded from below (Burago et al., 1992). This space does not have unique geodesics and objects like the Fréchet mean are not unique (Turner et al., 2014). The geometry and complicated structure of the persistence diagrams are an impediment to using the PHT in standard regression models, such as linear mixed models.

Our motivation for defining the SECT is that it contains the same information as the PHT but is a continuous, piecewise linear function and is an element in the Hilbert space $\mathbf{L}^2(\mathbf{R})$.

The Smooth Euler Characteristic Transform. The SECT is based on the Euler characteristic (EC), a common yet important topological invariant that comes up in many branches of mathematics. Classically, it is known to be of importance in polyhedral combinatorics and algebraic topology, and therefore in TDA.

Definition 2.3.2. The Euler characteristic (EC) χ for a finite simplicial complex K^d for $d = 3$ is defined by:

$$\chi(K^3) = V - E + F, \tag{3}$$

where V, E, and F are the numbers of vertices, edges, and faces, respectively.

Important probabilistic results based on the EC in the context of Gaussian random fields have also been established (Adler, 2010; Taylor and Adler, 2003; Adler and Taylor, 2007), and used in applications (Adler et al., 2014). In homology and persistent homology, the EC counts the Betti numbers β_k in an alternating sum.

The EC curve is constructed by tracking the progression of the EC as a function with respect to a filtration $\mathcal{K}$. In the context of closed, compact subsets (shapes) $M \subset \mathbf{R}^3$ represented by finite simplicial complexes K, we consider the filtration (1) via the height function (2) and denote the extremal heights from this filtration in the direction $\nu \in S^2$ by

$$\begin{aligned} a_\nu &:= \min\{r_\nu(x), x \in K\}, \\ b_\nu &:= \max\{r_\nu(x), x \in K\}. \end{aligned}$$

Definition 2.3.3. Let K_ν^x denote the simplicial complex that represents the closed, compact subset $M_\nu^x \subseteq M \subset \mathbf{R}^3$ generated by the sublevel set filtration (1), defined by the height function $r_\nu(x)$ in (2) for varying x, for a fixed unit direction vector $\nu \in S^2$. The *EC curve* is defined by

$$\begin{aligned} \chi_\nu^K : [a_\nu, b_\nu] &\to \mathbf{Z} \subset \mathbf{R} \\ x &\mapsto \chi\big(K_\nu^x\big). \end{aligned} \tag{4}$$

The EC curve tracks the evolution of the EC up to (and including) the largest subcomplex of M contained in the sublevel set $r_\nu^{-1}\big((-\infty, x]\big)$. See Figure 5 for an illustration of the EC curve. In considering a directional sweep over the surface of the sphere S^2, and calculating the corresponding EC curves of the finite simplicial complex representations of M for every direction $\nu \in S^2$, the *Euler characteristic transform (ECT)* (Turner et al., 2014) is defined as follows:

$$\begin{aligned} \mathrm{ECT}(M) : S^{d-1} &\to \mathbf{Z}^{\mathbf{R}} \\ \nu &\mapsto \chi\big(M(x, \nu)\big). \end{aligned} \tag{5}$$

Notice that the EC curve (4) and its corresponding ECT (5) are piecewise constant, integer-valued functions. The numerous discontinuities will affect the stability of this representation — this is visually illustrated in Figure 5(c). We therefore propose a reformulation of the ECT (5) to allow for computational tractability and statistical analyses, by smoothing the function via the following procedure. First, take the mean value of the EC curve $\bar{\chi}_\nu^K$ over $[a_\nu, b_\nu]$, and then subtract it from the value of the EC curve $\chi_\nu^K(x)$ at every $x \in [a_\nu, b_\nu]$. The result is a centered EC curve in the direction $\nu \in S^2$,

$$\begin{aligned} Z_\nu^K : [a_\nu, b_\nu] &\to \mathbf{R} \\ x &\mapsto \chi_\nu^K(x) - \bar{\chi}_\nu^K. \end{aligned} \tag{6}$$

Here, we denote the value of Z_ν^K to be zero outside the interval $[a_\nu, b_\nu]$. Through the cumulation of these results, we obtain the following construct:

Definition 2.3.4. The *centered, cumulative Euler characteristic curve*, or *smoothed Euler characteristic curve (SEC)*, for a fixed direction $\nu \in S^{d-1}$, is defined for all $y \in \mathbf{R}$ as

$$\begin{aligned} \mathrm{SEC}(M) : \mathbf{R} &\to \mathbf{L}^2 \\ F_\nu^K(y) &:= \int_{-\infty}^{y} Z_\nu^K(x)dx. \end{aligned} \tag{7}$$

The SEC is a continuous, piecewise linear function with compact support $[a_\nu, b_\nu]$, by construction. It is therefore an element of the Hilbert space $\mathbf{L}^2$ of square integrable functions on $\mathbf{R}$. The counterpart to Figure 5(c), smoothed by the procedure resulting in the SEC, is visually illustrated in Figure 5(d).

We now formally define the smooth Euler characteristic transform.

Definition 2.3.5. The *smooth Euler characteristic transform (SECT)* for a simplicial complex K of a shape M is the map

$$\begin{aligned} \text{SECT} : \{K, S^{d-1}\} &\to L^2[a_\nu, b_\nu] \\ \nu &\mapsto F_\nu^K(b_\nu) \end{aligned} \tag{8}$$

for all $\nu \in S^{d-1}$. Each curve F_ν^K is also an element in the Hilbert space $\mathbf{L}^2$. The following metric can therefore be used to define distances between two meshes K_1 and K_2:

$$\text{dist}_{\mathcal{M}_d}^{\text{SECT}}(K_1, K_2) := \left(\int_{S^{d-1}} \|F_\nu^{K_1} - F_\nu^{K_2}\|^2 d\nu \right)^{1/2}. \tag{9}$$

The advantage of the SECT over the PHT is that the SECT summaries are a collection of curves and has a Hilbert space structure, which means that their structure allows for quantitative comparisons using the full scope of statistical methdology. The SECT is also an injective map and the following corollary follows immediately from Theorem 3.1 in Turner et al. (2014).

Corollary 2.3.6. *The smooth Euler characteristic transform is injective when the domain is $\mathcal{M}_d$ for $d = 2, 3$.*

It is important to note here that enough directions $\nu \in S^{d-1}$ must be taken for this corollary to hold, since for any one fixed direction, it is not true that the EC curve (upon which the SECT construction depends) is injective. An illustration of this fact is depicted in Figure 6. To determine the number of directions to use for our application to GBM data, we performed a sensitivity analysis of many different combinations of numbers of directions and sublevel sets, and found our prediction results to be reasonably robust to our final choice of numerical parameters, given in Section 4.

3 Linear Mixed Models to Predict Clinical Outcomes

In this section, we specify the Bayesian linear mixed model (LMM) used to predict clinical outcomes based on a collection of mRNA gene expression measurements and morphometric, volumetric, and topological features based features of MRI scans. The model detailed here is similar to previous Bayesian LMMs used in genomic studies (Ishwaran and Rao, 2005; Guan and Stephens, 2011; Zhou et al., 2013). For more relevant background, see George and McCulloch (1993), Brown et al. (1998), and Barbieri and Berger (2004). The main advantage of the Bayesian framework is that it takes into account of uncertainty in parameter estimates when making predictive inferences.

3.1 Bayesian Linear Mixed Models

We now provide the LMM in which variance components are used to model the random effects of gene expression and tumor morphometrics, volumetrics, and topology

$$\mathbf{y} = \mathbf{g} + \mathbf{s} + \mathbf{m} + \mathbf{v} + \boldsymbol{\varepsilon}, \quad \boldsymbol{\varepsilon} \sim \text{MVN}(\mathbf{0}_n, \tau^{-1}\mathbf{I}_n), \tag{10}$$

where each component is assumed to come from the following distributions

$$\mathbf{g} \sim \text{MVN}(\mathbf{0}_n, \sigma_g^2 \mathbf{G}) \quad (11) \qquad \mathbf{m} \sim \text{MVN}(\mathbf{0}_n, \sigma_m^2 \mathbf{M}) \quad (13)$$

$$\mathbf{s} \sim \text{MVN}(\mathbf{0}_n, \sigma_s^2 \mathbf{S}) \quad (12) \qquad \mathbf{v} \sim \text{MVN}(\mathbf{0}_n, \sigma_v^2 \mathbf{V}). \quad (14)$$

In the above specification, $\mathbf{y}$ denotes an n-dimensional vector of clinical outcomes. We will assume that the residual variance is modeled by $\boldsymbol{\varepsilon}$, which is multivariate normal with mean zero residual inverse variance τ. The term $\mathbf{g}$ represents an n-dimensional vector of normally distributed random effects with known $n \times n$ covariance matrix $\mathbf{G} = \mathbf{X}\mathbf{X}^\intercal / p_g$, where $\mathbf{X}$ denotes an $n \times p_g$ genotype matrix of p_g gene expression measurements. $\mathbf{G}$ is commonly referred to as a genetic similarity matrix (GSM) and models the genomic correlations between individuals scaled by the total number of measured markers. Similarly, $\mathbf{s}$ is also an n-dimensional vector of normally distributed random effects with known $n \times n$ covariance matrix $\mathbf{S} = \mathbf{E}\mathbf{E}^\intercal / p_s$, where $\mathbf{E}$ is an $n \times p_s$ matrix containing the SECT summaries for each individual's MRI scan and p_s is the length of the topological summary vector for each individual. Here, $\mathbf{S}$ may be thought of as a GSM that captures the similarity of the tumor shape between individuals. Lastly, the random effects $\mathbf{m}$ and $\mathbf{v}$ model the variance of morphometric and volumetric features, respectively, where the interpretation of covariance matrices $\mathbf{M}$ and $\mathbf{V}$ is very similar to that of $\mathbf{S}$.

The motivation behind including each of these random components in (10) is to model tumor heterogeneity at both the molecular level through $\mathbf{g}$, as well as at the physiological level through $\mathbf{s}$, $\mathbf{m}$, and $\mathbf{v}$. The argument for considering tumor heterogeneity when predicting clinical responses is that there is overwhelming evidence that even tumors of the same type can exhibit significant distinct molecular and geometric behavior in different patients (Alizadeh et al., 2015).

We will consider variations of the model specified in equation (10) with the objective of examining whether the SECT and topological summaries can improve prediction accuracy for clinical outcomes — as opposed to the more standard biomarkers of gene expression and morphometric/volumetric features. To this end, we specify twelve models that can be clustered into distinct groups based on the data they include.

(1) $\mathbf{y} = \mathbf{g} + \boldsymbol{\varepsilon}$

(2) $\mathbf{y} = \mathbf{g} + \mathbf{m} + \boldsymbol{\varepsilon}$

(3) $\mathbf{y} = \mathbf{g} + \mathbf{v} + \boldsymbol{\varepsilon}$

(4) $\mathbf{y} = \mathbf{g} + \mathbf{m} + \mathbf{v} + \boldsymbol{\varepsilon}$

(5) $\mathbf{y} = \mathbf{m} + \boldsymbol{\varepsilon}$

(6) $\mathbf{y} = \mathbf{v} + \boldsymbol{\varepsilon}$

(7) $\mathbf{y} = \mathbf{m} + \mathbf{v} + \boldsymbol{\varepsilon}$

(8) $\mathbf{y} = \mathbf{s} + \boldsymbol{\varepsilon}$

(9) $\mathbf{y} = \mathbf{s} + \mathbf{g} + \boldsymbol{\varepsilon}$

(10) $\mathbf{y} = \mathbf{s} + \mathbf{m} + \boldsymbol{\varepsilon}$

(11) $\mathbf{y} = \mathbf{s} + \mathbf{v} + \boldsymbol{\varepsilon}$

(12) $\mathbf{y} = \mathbf{s} + \mathbf{m} + \mathbf{v} + \boldsymbol{\varepsilon}$

Briefly, Model 1 only includes gene expression data, Models 2-4 include both gene expression and geometric features, Models 5-7 include only geometric features, and Models 8-12 all include topological features via the SECT. A more detailed description for each of these models can be found in Table 1. For the rest of this section, we will state prior specifications and outline posterior sampling schemes for the complete LMM described in (10) — but, note that any of the twelve model variations detailed above may easily be adapted.

3.2 Prior and Hyper-prior Specifications

Given the model representation in (10), we take a Bayesian approach and assume that each of the variance components come from the following conjugate distribution

$$\tau, \sigma_*^{-2} \sim \Gamma(\kappa_1, \kappa_2) \tag{15}$$

where $* = \{g, s, m, v\}$, and Γ is used to denote a gamma distribution with κ_1 and κ_2 being the shape and rate parameters, respectively. When conducting posterior inference, we will exclusively consider the posterior distribution that arises in the limits $\kappa_1 \to 0$ and $\kappa_2 \to 0$. We note that while these limits correspond to improper priors, the resulting posteriors are proper, and most importantly, they scale appropriately with shifting or scaling of the phenotype vector $\mathbf{y}$ (Servin and Stephens, 2007). In other words, conclusions will be unaffected by changing the units of measurement of the phenotype (Zhou et al., 2013). This property is desirable in our setting because the phenotypic outcomes are assumed to be normalized. Moreover, in our particular application to GBM, the phenotypic outcomes are being characterized by the physical traits of the tumor, some of which are quantified topologically and therefore are also invariant to scaling and shifting. This intersection of the two fields strengthens the validity of our methodology in using this particular Bayesian analysis to topological quantifications.

3.3 Posterior Inference and Sampling

Given the full model, we use Markov chain Monte Carlo (MCMC) via a Gibbs sampler to obtain approximate samples from the joint posterior of the all parameters given the observed data. Specifically, posterior samples of $\boldsymbol{\Theta} = \{\mathbf{g}, \mathbf{s}, \mathbf{m}, \mathbf{v}, \tau, \sigma_g^2, \sigma_s^2, \sigma_m^2, \sigma_v^2\}$ may be obtained by using the following closed form conditional densities:

(1) $\mathbf{g} \,|\, \mathbf{y}, \boldsymbol{\Theta}_{-\mathbf{g}} \sim \text{MVN}(\boldsymbol{\mu}^*, \boldsymbol{\Sigma}^*)$
where $\boldsymbol{\mu}^* = \tau\boldsymbol{\Sigma}^*(\mathbf{y} - \mathbf{s} - \mathbf{m} - \mathbf{v})$ and $\boldsymbol{\Sigma}^* = \tau^{-1}\sigma_g^2(\tau^{-1}\mathbf{G} + \sigma_g^2\mathbf{I}_n)^{-1}$;

(2) $\mathbf{s} \,|\, \mathbf{y}, \boldsymbol{\Theta}_{-\mathbf{s}} \sim \text{MVN}(\boldsymbol{\mu}^*, \boldsymbol{\Sigma}^*)$
where $\boldsymbol{\mu}^* = \tau\boldsymbol{\Sigma}^*(\mathbf{y} - \mathbf{g} - \mathbf{m} - \mathbf{v})$ and $\boldsymbol{\Sigma}^* = \tau^{-1}\sigma_s^2(\tau^{-1}\mathbf{S} + \sigma_s^2\mathbf{I}_n)^{-1}$;

(3) $\mathbf{m} \,|\, \mathbf{y}, \boldsymbol{\Theta}_{-\mathbf{m}} \sim \text{MVN}(\boldsymbol{\mu}^*, \boldsymbol{\Sigma}^*)$
where $\boldsymbol{\mu}^* = \tau\boldsymbol{\Sigma}^*(\mathbf{y} - \mathbf{g} - \mathbf{s} - \mathbf{v})$ and $\boldsymbol{\Sigma}^* = \tau^{-1}\sigma_m^2(\tau^{-1}\mathbf{M} + \sigma_m^2\mathbf{I}_n)^{-1}$;

(4) $\mathbf{v} \,|\, \mathbf{y}, \boldsymbol{\Theta}_{-\mathbf{v}} \sim \text{MVN}(\boldsymbol{\mu}^*, \boldsymbol{\Sigma}^*)$
where $\boldsymbol{\mu}^* = \tau\boldsymbol{\Sigma}^*(\mathbf{y} - \mathbf{g} - \mathbf{s} - \mathbf{m})$ and $\boldsymbol{\Sigma}^* = \tau^{-1}\sigma_v^2(\tau^{-1}\mathbf{V} + \sigma_v^2\mathbf{I}_n)^{-1}$;

(5) $\tau \,|\, \mathbf{y}, \boldsymbol{\Theta}_{-\tau} \sim \Gamma(n/2, \mathbf{y}^\intercal\mathbf{y}/2)$;

(6) $\sigma_g^2 \,|\, \mathbf{y}, \boldsymbol{\Theta}_{-\sigma_g^2} \sim \Gamma(n/2, \mathbf{g}^\intercal\mathbf{G}^{-1}\mathbf{g}/2)$;

(7) $\sigma_s^2 \,|\, \mathbf{y}, \boldsymbol{\Theta}_{-\sigma_s^2} \sim \Gamma(n/2, \mathbf{s}^\intercal\mathbf{S}^{-1}\mathbf{s}/2)$;

(8) $\sigma_m^2 \,|\, \mathbf{y}, \boldsymbol{\Theta}_{-\sigma_m^2} \sim \Gamma(n/2, \mathbf{m}^\intercal\mathbf{M}^{-1}\mathbf{m}/2)$;

(9) $\sigma_v^2 \,|\, \mathbf{y}, \boldsymbol{\Theta}_{-\sigma_v^2} \sim \Gamma(n/2, \mathbf{v}^\intercal\mathbf{V}^{-1}\mathbf{v}/2)$.

Here, we denote $\boldsymbol{\Theta}_{-j}$ to be the vector $\boldsymbol{\Theta}$ without parameter j. Iterating the above procedure T times results in a desired set of posterior draws $\{\hat{\boldsymbol{\Theta}}^{(t)}\}_{t=1}^T$ with which posterior inference maybe conducted. In this work, we will exclusively be concerned with performing phenotypic prediction.

3.4 Conditional Prediction of Unobserved Phenotypes

We now formally define the conditional predicted response for a new and unobserved patient. Given a new patient's genotypes $\mathbf{X}^*$, and the corresponding tumor shape traits computed from the patient's MRI scans, samples from the posterior predictive distribution of $\mathbf{y}^*$ are drawn as follows

$$\mathbb{E}[\mathbf{y}^* \,|\, \mathbf{X}^*, \hat{\mathbf{\Theta}}] = \int \mathbf{y}^* p(\mathbf{y}^* \,|\, \mathbf{X}^*, \hat{\mathbf{\Theta}}) d\mathbf{y}^*. \tag{16}$$

In practice, this integral is analytically computed by simply plugging in the the posterior estimates of the random effects in the expression for the conditional expectation. Note that marginal (*i.e.* population averaged) prediction is different than conditional (*i.e.* tumor shape class specific) prediction. In our context, marginal prediction represents population strata defined by effects of a patient's gene expression, whereas conditional predictions express comparisons holding the tumor shape specific random effects constant (Skrondal and Rabe-Hesketh, 2009).

The justification for exclusively considering conditional predictions for unobserved phenotypes is that we may assume that every new unobserved patient will have an image of their tumor taken during diagnosis. From a medical perspective, it is generally unlikely that a patient with cancer, such as GBM, will have been invasively genotyped without having first done a noninvasive MRI scan. Hence, tumor shape traits for patients with unobserved phenotypes will always be available.

4 Application: Predicting Clinical Outcomes in Glioblastoma

The main objective to our statistical analysis is to understand which of the four features among gene expression, morphometric, volumetric, and topological features, or which combination of these features, are the best predictors for two clinical outcomes: disease free survival (DFS) and overall survival (OS).

Gene expression is often used in cancer genomics as an assay to predict phenotypes and clinical outcomes. More recently, radiogenomic studies have indicated associations between geometric features extracted from MRIs and gene expression levels with patient prognosis (Akbari et al., 2014; Mazurowski et al., 2014; Macyszyn et al., 2016; Law et al., 2006; Pope et al., 2012; Mazurowski et al., 2013; Li et al., 2012; Gutman et al., 2013; Chang et al., 2013). For instance, certain imaging modalities allow for the detection of necrotic regions, typically found in the anoxic centers of tumors (Mohammadi et al., 2016; Gutman et al., 2015). Clinical studies of GBMs have indicated that prognosis worsens as the degree of necrosis increases (Raza et al., 2002; Lacroix et al., 2001; Hammoud et al., 1996). Similarly, characteristics such as relative tumor blood volume have been used to identify brain tumors lacking epidermal growth factor receptor variant III (EGFRvIII) mutations — an increasingly relevant biomarker in the optimization of GBM therapy (Tykocinski et al., 2012). As a result, radiological imaging of GBM patients has become a powerful noninvasive tool for prediction of clinical outcome.

Our motivation for applying the SECT to images of GBMs is to study the performance of the shape of the tumor as a predictor of clinical outcome. We hypothesize that the shape of the tumor may be a better indicator of clinical prognosis than gene expression. Gene expression is known to be highly variable, particularly in GBM (Verhaak et al., 2010), while physical traits of the tumor are comparatively more stable. Volumetric, morphometric, and topological features are quantities that capture the physical traits (shape) of the tumor. Moreover, we suspect that the SECT, which captures the full shape information of the tumor, may outperform the standard geometric and morphometric quantities in prediction of clinical outcome, as well as in robustness to metric assumptions.

In our application to GBM, the robustness of the SECT to choice of metric is particularly relevant because the geometric structure of the brain is known to be fibrous — meaning that the brain is made up of, and connected by, cerebral fiber pathways (Wedeen et al., 2012). This brings into the question of the validity of assuming a usual Euclidean metric. Both volumetric and morphometric analyses require the specification of a metric, and in the case where the usual assumption of a Euclidean metric does not apply, one must be constructed or assumed, which is not always a straightforward task. Moreover, in fibrous settings, there is also the possibility for the further requirement of defining a geodesic. Examining topological properties, as opposed to metric-based properties, bypasses these technical difficulties, which also bypasses the introduction of statistical confounders associated with erroneous assumptions of metric or geodesic, or measurement errors.

Altogether, incorporating a topological measure that is not based on a metric results in the flexibility to compare tumors of different sizes more seamlessly. Subsequently, this also implicitly allows for comparisons between different stages of the disease to be examined without needing to account for time of progression. We hypothesize that these flexible characteristics will favor the SECT as a better predictor of prognosis and survival.

4.1 Radiogenomic Data

MRIs of primary GBM tumors were collected from 92 patients archived by the The Cancer Imaging Archive (TCIA) (Clark et al., 2013), which is a publicly accessible data repository of medical images of cancer patients with matched data in The Cancer Genome Atlas (TCGA) — a collection of a variety of genomic and clinical data for 33 types of cancer. The 92 patients were selected based on two sets of criteria, namely, that they had post-contrast T1 axial MRIs taken at the time of their diagnosis, and that they had available matching (mRNA) gene expression data and clinical correlates (*e.g.* recorded DFS and OS) on cBioPortal (Gao et al., 2013). There are two key factors that influenced our decision to use this particular dataset. First, T1-weighted MRI with Gadolinium contrast (T1C) is a commonly-used imaging modality that can assay lesions with vascular activity (Adin et al., 2015). Second, exclusively using MRIs taken at the time of diagnosis allows us to avoid any potential confounding factors related to treatment effects that may manifest on postoperative imaging (Macyszyn et al., 2016). In particular, considering patients that have undergone different treatment regimens and procedures could introduce false positives into the model.

We segmented the TCIA MRI images using a computer-assisted segmentation program to extract tumor lesions from the surrounding brain tissue, which first converts MRI images to a grayscale, and then thresholds to generate binary images. Morphological segmentation is then applied to delineate connected components. More specifically, the program selects contours corresponding to enhanced tumor lesions, which are lighter than healthy brain tissue. As previously noted, necrosis presents as dark regions nested within the indicated lesion. An example of the raw image obtained from TCIA is given in Figure 7(a). The final segmented result is given in Figure 7(b).

Gene Expression Data. The 92 TCGA samples was were preprocessed using MAS5.0 (Irizarry et al., 2003) to normalize the mRNA gene expression data and remove genes that did not vary, or that posed concerns about the accuracy of the hybridization in the assay. This resulted in 9215 of the original 18901 genes, $p_g = 9215$.

Morphometric Data. The same morphometric features outlined in Chang et al. (2011) and Han et al. (2010) were used in our study. The pipeline to compute these features is outlined in detail in

Chang et al. (2011). Briefly, the first step is to segment the image. The second step is to extract features from the segmented image. This resulted in the number of features corresponding to shape and texture, $p_m = 212$.

Volumetric Data. From the segmented images, we also calculated the following volumetric features: the enhancing volume for each slice, summed over lesions in the multifocal case; the core volume of the enhancing and necrotic regions; the longest diameter of the lesions; and the shape factor, which we define to be the longest diameter divided by the diameter of a sphere of the same volume. The total number of features was $p_v = 5$.

Topological Data. Among the 92 segmented images, each consisted of 23-25 slices of two dimensional greyscale images (the exact number of slices varies by patient). For the binary images, we compute a two-dimensional SECT for each slice over 72 directions evenly sampled over $[0, 2\pi]$. Each of the $N = 72$ smooth EC curves are vectors of length $q = 100$, the fixed number of sublevel sets. We average the smooth EC curves for a fixed direction across all slices, so if we index directions as ν and slices as q we first compute 72 EC curves $\mathbf{e} = \{\mathbf{c}_\nu\}_{\nu=1}^N$ by averaging over all L the slices:

$$\bar{\mathbf{c}}_\nu = \frac{1}{L}\sum_{\ell=1}^{L} \mathbf{c}_{\nu\ell},$$

where $\mathbf{c}_{\nu\ell}$ is the smooth EC curve for the ℓ-th slice in direction ν. For an image from patient i, we obtain 72 vectors of length 100 which we concatenate into one vector of length $q \times N$ which we denote as $\mathbf{e}_i$. Given n patients, the imaging data will be represented as an $n \times p_s$ matrix which we denote as $\mathbf{E} = [\mathbf{e}_1 \cdots \mathbf{e}_n]$, where $p_s = q \times N$.

Clinical Phenotypes. We considered two clinical outcomes.

- Disease Free Survival (DFS): The period after a successful treatment during which there are no signs or symptoms of the cancer that was treated.
- Overall Survival (OS): The entire period after the start of treatment during which the cancer patient is still alive.

DFS is more commonly used over OS in adjuvant cancer clinical trials, because it offers earlier presentation of data (Sargent et al., 2005). In particular, this stems from the idea that events due to disease recurrence occur earlier than death from disease (Birgisson et al., 2011).

4.2 Prediction Results

In our statistical analyses, we compared the predictive accuracy for both clinical outcomes for each type of data feature: gene expression, morphometric, volumetric, and topological summaries. Our findings show that for DFS, the topological features result in the most accurate predictions, while gene expression is the least informative of the features. For OS, the volumetric features are the best predictive indicators.

As measures of predictive performance, we used two metrics described in Hahn et al. (2013) to compare out-of-sample predictive accuracy: root mean square error of prediction (RMSEP); and the tabulated frequency for which a given method exhibits the lowest RMSEP, which we denote as Pr[Optimal]. To perform the prediction, we split the data into 80% training and 20% out-of-sample test sets, and ran 500 of these splits for both DFS and OS. Numerical results under both metrics

are presented in Table 2. We treated the gene expression only model as a baseline (Model 1 in Table 2) and report the RMSEP of all the other methods relative to Model 1 (see Figure 8).

Models with Geometric Features. In our comparison study, we were able to replicate previous findings that morphometric or volumetric features (summarized as geometric features) are useful predictors of outcome phenotypes: This was reflected in the mixed effects models, since Models 5-7 exhibited robustly low RMSEPs in predicting both DFS and OS. This result is consistent with other radiogenomics studies that found geometric traits such as core volume, longest diameter, and shape factor of the largest lesion to be better predictors of clinical outcome than gene expression (Gutman et al., 2013; Hammoud et al., 1996; Itakura et al., 2015; Mazurowski et al., 2014).

Models with Topological Features. The random effects model that included only topological features was able to most accurately predict DFS (RMSEP = 0.897 and Pr[Optimal] = 0.292). Recall that DFS is defined as as the time period between initial treatment and first recurrence of the disease. DFS is arguably the most important clinical outcome for patients with GBM because recurrence rates are high (∼90%) (Weller et al., 2012). Our findings suggest that the topological shape features captured by the SECT contains more predictive information about GBM relapse than both gene expression, geometric features.

One possible explanation for our results is that there may be correlations between the topological features of tumors, and tumor heterogeneity potentially arising from the activation of different molecular recurrence mechanisms. An example of this correlation occurs in certain multicentric and multifocal tumors — tumors with lesions in opposing hemispheres of the brain that arise from the same oncogenic effects — that exhibit heterogeneity within only one hemisphere. This variation can be clinically relevant. In Lee et al. (2016), a case study is described where a multicentric tumor relapsed in only one hemisphere of the brain, and the relapse took the form of multifocal lesions. The authors then go on to show that clinical prognostics correlate directly with the multicentricity and multifocality of tumors, and they draw connections between these topological traits and the mutation status of oncogenic relapse drivers such as *PIK3CA*. This provides evidence that the existence of underlying characteristics of resistance and relapse mechanisms of the disease go beyond the simple consideration of proximity in a geometric sense. For instance, these characteristics may be due to ambient effects inherent to the particular hemisphere of the brain. The prediction results we present in this work suggest that the topological features extracted by the SECT may be better than simple geometric summaries at providing insight into biological phenomena at the molecular level.

Predicting DFS vs. OS. While the random effects models that included topological features predicted DFS most accurately, the random effects models that included geometric features were the most accurate in predicting OS. We conjecture that the discrepancy in predictive performance is due to the nature of the clinical outcome measures.

DFS, as mentioned previously, is a prognostic measure that depends on relapse, which corresponds to the existence of the disease after initial treatment. This notion is better captured by topological features, which in our cancer application, details the presence of tumors. Measurements that encompass information on the aggressiveness of the disease are not as relevant as those that measure sheer existence. This corresponds to a topological trait, rather than a volumetric or morphometric one.

OS, on the other hand, is a prognostic measure that depends on survival of the patient, which is better described by features that capture the aggressiveness of the disease. There have been studies

that show a correlation between volumetric features and biological aggressiveness of tumors (Talos et al., 2007; Leong et al., 2015). Geometric features, such as size and location of the tumor and especially its proximity to crucial regions of the brain, give some measure about the aggressiveness of the disease and therefore directly impact survival of the patient.

5 Discussion

In this paper we introduced the smooth Euler characteristic transform (SECT) as a topological summary of shapes designed to integrate shape information into standard statistical models. Here, we used the SECT features in a linear mixed model to predict clinical outcomes based on gene expression and imaging data. We found that the topological characteristics captured by the SECT were the most accurate predictors for disease free survival. More specifically, the topological features outperformed gene expression measurements, as well as volumetric and morphometric features.

There are several interesting future directions and open problems involving the use of topological features, such as the SECT, in radiogenomics. We state four particular directions below.

Shape Reconstruction. It would be useful to infer which particular regions of the tumor are most relevant to predicting outcome. Standard variable selection methods can be used to infer the directions and segments of the Euler curves most relevant to prediction. An important open problem is to recover or reconstruct a shape from the SECT, or part of a shape from a subset of SECT. We have some preliminary results indicating that an algorithm to reconstruct the shape, or a region of the shape, from topological summaries such as the SECT is possible. Overlaying significant regions of interest with molecular markers and signaling pathways would be interesting to be able to further understand the exact mechanics of the disease.

The Shape of a Tumor and Disease Etiology. The distance measure for the SECT stated in equation (9) provides a framework for comparing the shapes of tumors, and correlating shape with molecular and clinical features. Understanding the effect of variation over tumor shapes on therapies, pre- and post-treatment, as well as differences between treatment strategies would provide useful information about different forms of GBM, and more generally, cancer. We conjecture that greater knowledge about the shape of a tumor may help in distinguishing true progression from pseudoprogression: progression is the growth of the tumor itself, while in pseudoprogression, the tumor is infiltrated by immune cells and other factors.

Integration With Other Features. There is evidence that epigenomic features, such as DNA methylation, provide predictive information on clinical prognosis and tumor heterogeneity (Zhang et al., 2015; Hansen et al., 2011). Methylation is also a more stable molecular marker than gene expression, and therefore may be a better predictor variable of outcome. The existence of correlations between methylation and imaging would provide a proxy measurement of the epigenome which is far less invasive.

Gene Set Enrichment Analysis Using Shape Statistics. An important procedure in cancer biology is to examine sets of genes that belong to a signaling pathway, and to compute the gene set score that captures dysregulation in the pathway (Subramanian et al., 2005; Drier et al., 2013; Edelman et al., 2008). It would of interest to probe whether variation in shape is correlated with pathway dysregulation.

Software and Data

Software to compute the ECT and SECT from images is publicly available from the Rabadán Lab GitHub repository `https://github.com/RabadanLab/SECT`. Posterior estimation via Gibbs sampling and prediction for the Bayesian LMM was carried out in R version 3.3.1 (R Core Team, 2016) using the publicly available BGLR software package (de los Campos et al., 2010; Crossa et al., 2014; Howard et al., 2014). The segmented images in addition to the gene expression, volumetric, and morphometric data as well as the scripts generating the figures and tables in the paper are also publicly available on the Rabadán Lab GitHub repository.

Acronyms used in the paper

- DFS: Disease free survival
- EC: Euler characteristic
- ECT: Euler characteristic transform
- GBM: Glioblastoma multiforme
- GSM: Genetic similarity matrix
- LMM: Linear mixed model
- MRI: Magnetic resonance imaging
- OS: Overall survival
- PHT: Persistent homology transform
- RMSEP: Root mean squared error of prediction
- SEC: Smooth Euler characteristic
- SECT: Smooth Euler characteristic transform
- TCGA: The Cancer Genome Atlas
- TCIA: The Cancer Imaging Archive
- TDA: Topological data analysis

Acknowledgements

L.C. is supported by the National Science Foundation Graduate Research Program under Grant No. DGF-1106401. A.M. and R.R. are supported by the National Cancer Institute Physical Sciences–Oncology Network (NCI PS–ON) under Grant No. 5U54CA193313-02; A.M. is the PI on Pilot Grant Subaward No. G11124. A.X.C. is supported by the Columbia University Medical Scientist Training Program (MSTP). S.M. would like to acknowledge the support of grants NSF IIS-1546331, NSF DMS-1418261, NSF IIS-1320357, NSF DMS-1045153, and NSF DMS-1613261. The authors wish to thank Mao Li (Donald Danforth Plant Science Center) for help with the formulation of code, as well as Francesco Abate and Jiguang Wang (Columbia University), and

Katharine Turner (Swiss Federal Institute of Technology) for helpful conversations and input on a previous version of the manuscript. The authors would also like to acknowledge The Cancer Imaging Archive and The Cancer Genome Atlas initiatives for making the imaging and the clinical data used in this study publicly available. Any opinions, findings, and conclusions or recommendations expressed in this material are those of the author(s) and do not necessarily reflect the views of any of the funders.

Supplemental Material

Table S1: Complete list of the morphometric and volumetric (*i.e.* geometric features) used in the prediction analysis presented in Section 4 (see https://github.com/RabadanLab/SECT).

Figures and Tables as Mentioned in Text

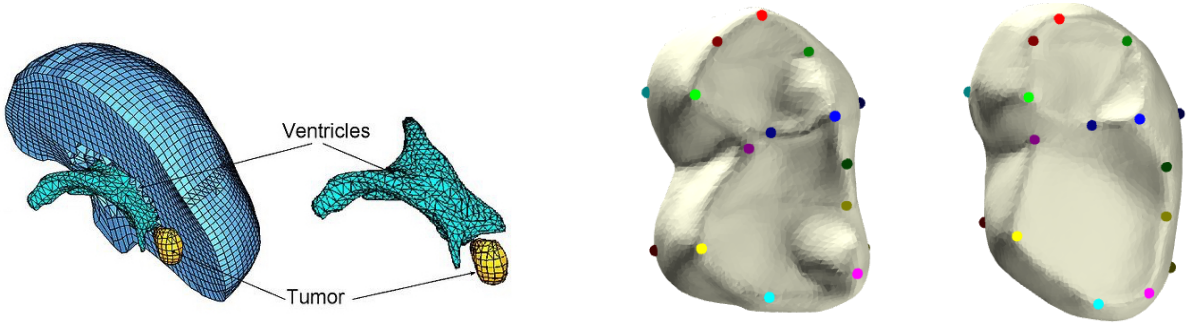

(a) (b)

Figure 1: (a) A mesh representation of a brain tumor and ventricles. (b) A landmark representation of two molars first published in Boyer et al. (2011).

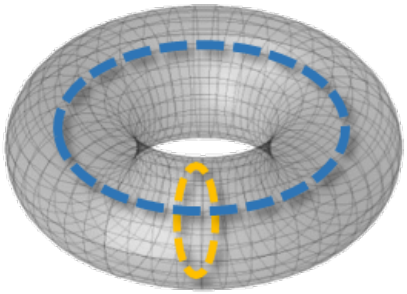

Figure 2: The 2-dimensional torus and its cycles. The torus has a single connected component and a single 2-cycle (the void locked inside the torus). In addition it has two distinct 1-dimensional cycles (or closed loops) represented by the two curves in the figure. Consequently the Betti numbers of the torus are $\beta_0 = 1, \beta_1 = 2, \beta_2 = 1$. This figure was first published in Bobrowski et al. (2017).

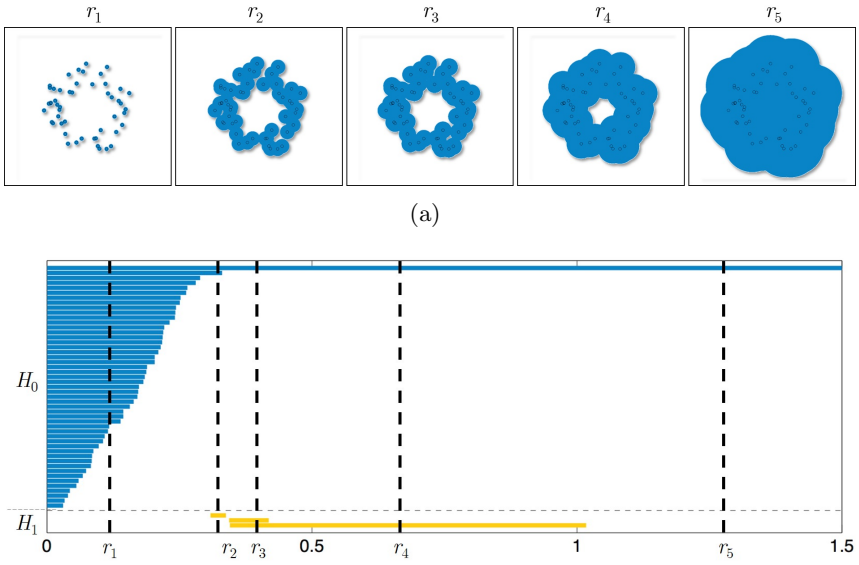

Figure 3: (a) X_r is a union of balls of radius r around a random set of $n = 50$ points, generated from a uniform distribution on an annulus in $\mathbf{R}^2$. Illustrated are five instances of X_r with different radius sizes. (b) The persistent homology of the filtration $\{X_r\}_{r=0}^{\infty}$. The x-axis is the radius of the balls, and the bars represent the homology features that are born and die. For H_0, we observe that at radius zero, the number of components is exactly n and as the radius increases, components merge (or die). The cycles show up later in this process. There are two bars that are significantly longer than the others (one in H_0 and one in H_1). These correspond to the true feature of the annulus. This figure was first published in Bobrowski et al. (2017).

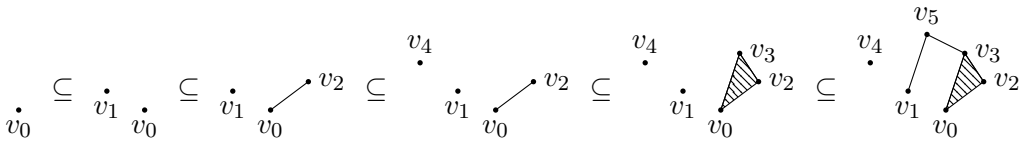

Figure 4: The filtration of K by height in direction ν. Each simplex is included at its maximal height. This figure was first published in Turner et al. (2014).

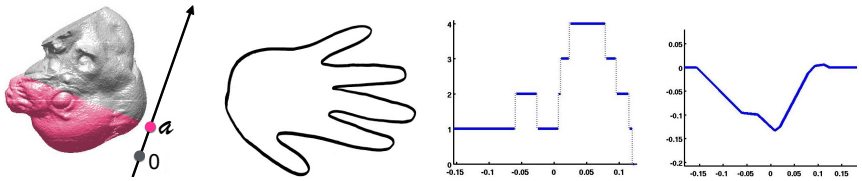

Figure 5: (a) Sublevel set of a mouse embryo head; (b) A 2D contour of a hand; (c) EC curve of the 2D contour of a hand; and (d) The associated smooth Euler characteristic curve.

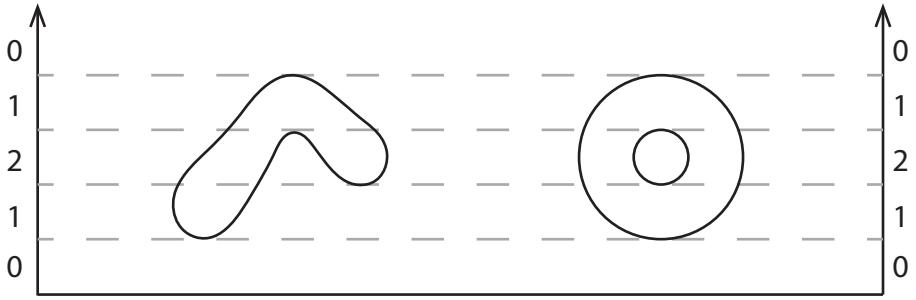

Figure 6: Counterexample for injectivity of the EC curve for a fixed direction: The vertical axis on both sides of the figure show the direction of the filtration of both shapes by height (sublevel set filtration). The numbers on the side of the axis show the evolution of the EC for both shapes. We see that although the EC changes in exactly the same manner for the filttration for both shapes, yielding identical ECTs for a fixed direction $\nu \in S^{d-1}$, the shapes that generate this ECT differ. It is important to note that enough directions must be considered for injectivity of the ECT and SECT to hold.

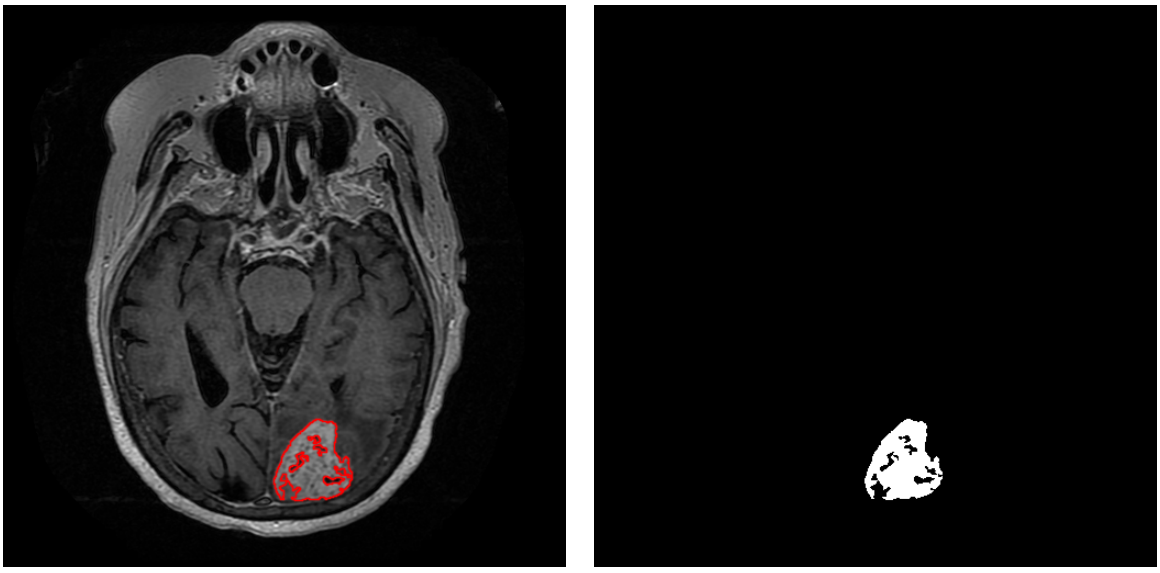

(a) Original MRI (b) Segmented MRI

Figure 7: Example of performance of the segmentation algorithm. (a) Original MRI from the TCIA and TCGA; (b) Final segmented image via the proposed segmentation algorithm.

	Index	Model Specification	Detailed Description
	1	$\mathbf{y} = \mathbf{g} + \boldsymbol{\varepsilon}$	Random effects model controlling for only gene expression data
Gene Expression Data + Geometric Features	2	$\mathbf{y} = \mathbf{g} + \mathbf{m} + \boldsymbol{\varepsilon}$	Random effects model controlling for molecular heterogeneity and morphometric features
	3	$\mathbf{y} = \mathbf{g} + \mathbf{v} + \boldsymbol{\varepsilon}$	Random effects model controlling for molecular heterogeneity and volumetric features
	4	$\mathbf{y} = \mathbf{g} + \mathbf{m} + \mathbf{v} + \boldsymbol{\varepsilon}$	Random effects model controlling for molecular heterogeneity, as well as morphometric and volumetric features
Geometric Features	5	$\mathbf{y} = \mathbf{m} + \boldsymbol{\varepsilon}$	Random effects model controlling for only morphometric features of MRIs
	6	$\mathbf{y} = \mathbf{v} + \boldsymbol{\varepsilon}$	Random effects model controlling for only volumetric features of MRIs
	7	$\mathbf{y} = \mathbf{m} + \mathbf{v} + \boldsymbol{\varepsilon}$	Random effects model controlling for both morphometric and volumetric features of MRIs
Topological Features	8***	$\mathbf{y} = \mathbf{s} + \boldsymbol{\varepsilon}$	Random effects model controlling for only the SECT of MRIs
	9***	$\mathbf{y} = \mathbf{s} + \mathbf{g} + \boldsymbol{\varepsilon}$	Random effects model controlling for molecular heterogeneity and topological features via the SECT
Topological + Geometric Features	10***	$\mathbf{y} = \mathbf{s} + \mathbf{m} + \boldsymbol{\varepsilon}$	Random effects model controlling for the SECT and morphometry of MRIs
	11***	$\mathbf{y} = \mathbf{s} + \mathbf{v} + \boldsymbol{\varepsilon}$	Random effects model controlling for the SECT and volume of MRIs
	12***	$\mathbf{y} = \mathbf{s} + \mathbf{m} + \mathbf{v} + \boldsymbol{\varepsilon}$	Random effects model controlling for the SECT, morphometry, and volume of MRIs

Table 1: Models considered when predicting disease free survival (DFS) and overall survival (OS) in patients with GBM. Model # 1, which only includes gene expression data is considered to be the baseline model. ***: Denotes models that incorporate topological information from the MRIs via the smooth Euler characteristic transform (SECT).

	Disease Free Survival		Overall Survival	
Model #	**RMSEP**	**Pr[Optimal]**	**RMSEP**	**Pr[Optimal]**
1	1.053 (0.018)	0.044	1.019 (0.031)	0.058
2	1.004 (0.018)	0.048	1.017 (0.032)	0.044
3	1.070 (0.018)	0.008	1.013 (0.032)	0.012
4	1.028 (0.018)	0.016	1.022 (0.033)	0.006
5	0.951 (0.018)	0.112	0.977 (0.033)	0.072
6	1.004 (0.018)	0.064	**0.947 (0.032)**	**0.282**
7	0.984 (0.018)	0.050	0.973 (0.033)	0.058
8***	0.913 (0.016)	0.150	1.039 (0.033)	0.020
9***	0.946 (0.016)	0.038	1.063 (0.032)	0.014
10***	**0.897 (0.016)**	**0.292**	1.028 (0.032)	0.098
11***	0.932 (0.016)	0.070	0.988 (0.029)	0.168
12***	0.918 (0.016)	0.108	0.989 (0.030)	0.168

Table 2: Results for predicting disease free survival (DFS) and overall survival (OS). The left hand panels shows comparisons of root mean squared errors of prediction (RMSEP) for the three considered models. The right hand panels detail the percentage of the time that a model exhibits the lowest RMSEP. This is denoted as Pr[Optimal]. All values in bold represent the method with the lowest RMSEP or the method that most frequently performs best, respectively. These values are based on 500 different 80-20 splits for each clinical outcome. Indexes under the Model # column correspond to the same models detailed in Table 1. Numbers in parentheses represent the standard errors of the RMSEP across these replicates for each model. ***: Denotes models that incorporate topological information from the MRIs via the smooth Euler characteristic transform (SECT).

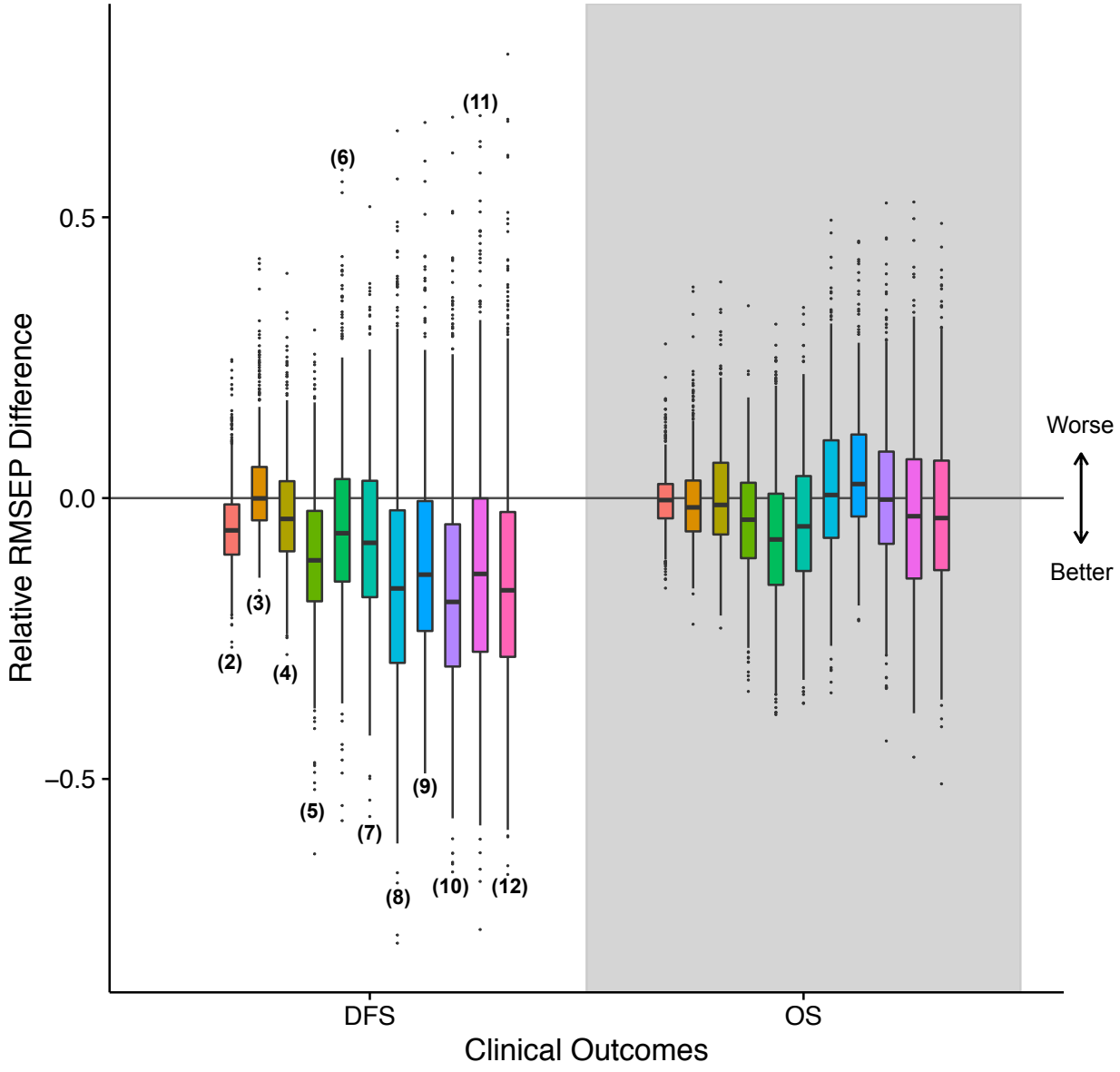

Figure 8: Relative prediction performance as compared with the gene expression only linear model for disease free and overall survival (DFS and OS, respectively). Performance is measured by the relative root mean squared error of prediction (RMSEP) difference, where a positive value indicates worse performance than Model #1: the linear model with only gene expression data (*i.e.* baseline model). The numbers attached to each box plot are indexes corresponding to the same models detailed in Table 1.

References

Adin, M. E., L. Kleinberg, D. Vaidya, E. Zan, S. Mirbagheri, and D. M. Yousem (2015). Hyperintense dentate nuclei on t1-weighted mri: Relation to repeat gadolinium administration. *American Journal of Neuroradiology 36*(10), 1859–1865.

Adler, R., K. Bartz, S. Kou, and A. Monod (2014). Estimating theresholding levels for random fields via euler characteristics. Under revision.

Adler, R. J. (2010). *The Geometry of Random Fields*. Society for Industrial and Applied Mathematics.

Adler, R. J. and J. E. Taylor (2007). *Random Fields and Geometry*. Springer monographs in mathematics. New York: Springer.

Akbari, H., L. Macyszyn, X. Da, R. L. Wolf, M. Bilello, R. Verma, D. M. O'Rourke, and C. Davatzikos (2014). Pattern analysis of dynamic susceptibility contrast-enhanced mr imaging demonstrates peritumoral tissue heterogeneity. *Radiology 273*(2), 502–510.

Al-Aifari, R., I. Daubechies, and Y. Lipman (2013). Continuous Procrustes Distance Between Two Surfaces. *Communications on Pure and Applied Mathematics 66*(6), 934–964.

Alizadeh, A. A., V. Aranda, A. Bardelli, C. Blanpain, C. Bock, C. Borowski, C. Caldas, A. Califano, M. Doherty, M. Elsner, M. Esteller, R. Fitzgerald, J. O. Korbel, P. Lichter, C. E. Mason, N. Navin, D. Pe'er, K. Polyak, C. W. M. Roberts, L. Siu, A. Snyder, H. Stower, C. Swanton, R. G. W. Verhaak, J. C. Zenklusen, J. Zuber, and J. Zucman-Rossi (2015). Toward understanding and exploiting tumor heterogeneity. *Nat Med 21*(8), 846–853.

Barbieri, M. M. and J. O. Berger (2004). Optimal predictive model selection. pp. 870–897.

Birgisson, H., U. Wallin, L. Holmberg, and B. Glimelius (2011). Survival endpoints in colorectal cancer and the effect of second primary other cancer on disease free survival. *BMC Cancer 11*(1), 438.

Bobrowski, O., S. Mukherjee, and J. E. Taylor (2017). Topological consistency via kernel estimation. *Bernoulli*, 288–328.

Bookstein, F. L. (1997). *Morphometric Tools for Landmark Data: Geometry and Biology*. Cambridge University Press.

Borsuk, K. (1948). On the imbedding of systems of compacta in simplicial complexes. *Fundamenta Mathematicae 35*(1), 217–234.

Boyer, D. M., Y. Lipman, E. St. Clair, J. Puente, B. A. Patel, T. Funkhouser, J. Jernvall, and I. Daubechies (2011). Algorithms to Automatically Quantify the Geometric Similarity of Anatomical Surfaces. *Proceedings of the National Academy of Sciences 108*(45), 18221–18226.

Boyer, D. M., J. Puente, J. T. Gladman, C. Glynn, S. Mukherjee, G. S. Yapuncich, and I. Daubechies (2015). A new fully automated approach for aligning and comparing shapes. *The Anatomical Record 298*(1), 249–276.

Brown, P. J., M. Vannucci, and T. Fearn (1998). Multivariate bayesian variable selection and prediction. *Journal of the Royal Statistical Society: Series B (Statistical Methodology) 60*(3), 627–641.

Bubenik, P. (2015). Statistical topological data analysis using persistence landscapes. *J. Mach. Learn. Res. 16*(1), 77–102.

Burago, Y., M. Gromov, and G. Perel'man (1992). A.D. Alexandrov spaces with curvature bounded below. *Russian Mathematical Surveys 47*(2), 1–58.

Carlsson, G. (2009). Topology and data. *Bull. Amer. Math. Soc. (N.S.) 46*(2), 255–308.

Carlsson, G. (2014). Topological pattern recognition for point cloud data. *Acta Numerica 23*, 289–368.

Chang, H., G. V. Fontenay, J. Han, G. Cong, F. L. Baehner, J. W. Gray, P. T. Spellman, and B. Parvin (2011). Morphometic analysis of tcga glioblastoma multiforme. *BMC Bioinformatics 12*(1), 484.

Chang, H., J. Han, A. Borowsky, L. Loss, J. W. Gray, P. T. Spellman, and B. Parvin (2013). Invariant delineation of nuclear architecture in glioblastoma multiforme for clinical and molecular association. *IEEE Transactions on Medical Imaging 32*(4), 670–682.

Clark, K., B. Vendt, K. Smith, J. Freymann, J. Kirby, P. Koppel, S. Moore, S. Phillips, D. Maffitt, M. Pringle, L. Tarbox, and F. Prior (2013). The cancer imaging archive (tcia): Maintaining and operating a public information repository. *Journal of Digital Imaging 26*(6), 1045–1057.

Crossa, J., P. Pérez, J. Hickey, J. Burgueño, L. Ornella, J. Cerón-Rojas, X. Zhang, S. Dreisigacker, R. Babu, Y. Li, D. Bonnett, and K. Mathews (2014). Genomic prediction in CIMMYT maize and wheat breeding programs. *Heredity 112*(1), 48–60.

de los Campos, G., D. Gianola, G. J. M. Rosa, K. A. Weigel, and J. Crossa (2010). Semi-parametric genomic-enabled prediction of genetic values using reproducing kernel Hilbert spaces methods. *Genetics Research (Cambridge) 92*(4), 295–308.

Drier, Y., M. Sheffer, and E. Domany (2013). Pathway-based personalized analysis of cancer. *Proceedings of the National Academy of Sciences 110*(16), 6388–6393.

Dryden, I. and K. Mardia (1998). *Statistical shape analysis*. Wiley Series in Probability and Statistics. Wiley.

Edelman, E. J., J. Guinney, J.-T. Chi, P. G. Febbo, and S. Mukherjee (2008). Modeling cancer progression via pathway dependencies. *PLoS Computational Biology 4*(2), 1–13.

Edelsbrunner, H., D. Letscher, and A. Zomorodian (2000). Topological persistence and simplification. In *Proceedings of the 41st Annual Symposium on Foundations of Computer Science*, FOCS'00, Washington, DC, USA. IEEE Computer Society.

Gao, J., B. A. Aksoy, U. Dogrusoz, G. Dresdner, B. Gross, S. O. Sumer, Y. Sun, A. Jacobsen, R. Sinha, E. Larsson, E. Cerami, C. Sander, and N. Schultz (2013). Integrative analysis of complex cancer genomics and clinical profiles using the cbioportal. *Science Signaling 6*(269).

Gao, T. (2015). *Hypoelliptic Diffusion Maps and Their Applications in Automated Geometric Morphometrics*. Ph. D. thesis, Duke University.

Gao, T., J. Brodzki, and S. Mukherjee (2016). The Geometry of Synchronization Problems and Learning Group Actions. *ArXiv e-prints*.

Gao, T., G. S. Yapuncich, I. Daubechies, S. Mukherjee, and D. M. Boyer (2016). Development and assessment of fully automated and globally transitive geometric morphometric methods, with application to a biological comparative dataset with high interspecific variation. *bioRxiv*.

George, E. I. and R. E. McCulloch (1993). Variable selection via gibbs sampling. *Journal of the American Statistical Association 88*(423), 881–889.

Gevaert, O., L. a. Mitchell, A. S. Achrol, J. Xu, S. Echegaray, G. K. Steinberg, S. H. Cheshier, S. Napel, G. Zaharchuk, and S. K. Plevritis (2014). Glioblastoma Multiforme: Exploratory Radiogenomic Analysis by Using Quantitative Image Features. *Radiology 273*(1), 131731.

Ghrist, R. (2008). Barcodes: the persistent topology of data. *Bull. Amer. Math. Soc. (N.S.) 45*(1), 61–75.

Guan, Y. and M. Stephens (2011). Bayesian variable selection regression for genome-wide association studies and other large-scale problems. *Annals of Applied Statistics 5*(3), 1780–1815.

Gutman, D. A., L. A. D. Cooper, S. N. Hwang, C. A. Holder, J. Gao, T. D. Aurora, W. D. Dunn, L. Scarpace, T. Mikkelsen, R. Jain, M. Wintermark, M. Jilwan, P. Raghavan, E. Huang, R. J. Clifford, P. Mongkolwat, V. Kleper, J. Freymann, J. Kirby, P. O. Zinn, C. S. Moreno, C. Jaffe, R. Colen, D. L. Rubin, J. Saltz, A. Flanders, and D. J. Brat (2013). Mr imaging predictors of molecular profile and survival: Multi-institutional study of the tcga glioblastoma data set. *Radiology 267*(2), 560–569.

Gutman, D. A., W. D. Dunn, P. Grossmann, L. A. D. Cooper, C. A. Holder, K. L. Ligon, B. M. Alexander, and H. J. W. L. Aerts (2015). Somatic mutations associated with mri-derived volumetric features in glioblastoma. *Neuroradiology 57*(12), 1227–1237.

Hahn, P., C. Carvalho, and S. Mukherjee (2013). Partial factor modeling: Predictor-dependent shrinkage for linear regression. *J. Am. Stat. Assoc. 808*, 999–1008.

Hammoud, M. A., R. Sawaya, W. Shi, P. F. Thall, and N. E. Leeds (1996). Prognostic significance of preoperative mri scans in glioblastoma multiforme. *J Neurooncol 27*(1), 65–73.

Han, J., H. Chang, K. Andarawewa, P. Yaswen, M. H. Barcellos-Hoff, and B. Parvin (2010). Multidimensional profiling of cell surface proteins and nuclear markers. *IEEE/ACM Trans. Comput. Biol. Bioinformatics 7*(1), 80–90.

Hansen, K. D., W. Timp, H. C. Bravo, S. Sabunciyan, B. Langmead, O. G. McDonald, B. Wen, H. Wu, Y. Liu, D. Diep, E. Briem, K. Zhang, R. A. Irizarry, and A. P. Feinberg (2011). Increased methylation variation in epigenetic domains across cancer types. *Nat Genet 43*(8), 768–775.

Hatcher, A. (2002). *Algebraic topology*. Cambridge University Press.

Holland, E. C. (2000). Glioblastoma multiforme: The terminator. *Proc Natl Acad Sci U S A 97*(12).

Howard, R., A. L. Carriquiry, and W. D. Beavis (2014). Parametric and nonparametric statistical methods for genomic selection of traits with additive and epistatic genetic architectures. *G3 (Bethesda) 4*(6), 1027–1046.

Irizarry, R., C. Hobbs, Y. Beazer-Barclay, K. Antonellis, U. Scherf, and T. Speed (2003). Exploration, normalization, and summaries of high density oligonucleotide array probe level data. *Biostatistics. 2*(4), 249–64.

Ishwaran, H. and J. S. Rao (2005). Spike and slab variable selection: Frequentist and Bayesian strategies. *Annals of Applied Statistics 33*(2), 730–773.

Itakura, H., A. S. Achrol, L. A. Mitchell, J. J. Loya, T. Liu, E. M. Westbroek, A. H. Feroze, S. Rodriguez, S. Echegaray, T. D. Azad, K. W. Yeom, S. Napel, D. L. Rubin, S. D. Chang, G. R. Harsh, and O. Gevaert (2015). Magnetic resonance image features identify glioblastoma phenotypic subtypes with distinct molecular pathway activities. *Science Translational Medicine 7*(303), 303ra138–303ra138.

Kendall, D. G. (1984). Shape manifolds, procrustean metrics, and complex projective spaces. *Bulletin of the London Mathematical Society 16*(2), 81–121.

Kim, J., I.-H. Lee, H. J. Cho, C.-K. Park, Y.-S. Jung, Y. Kim, S. H. Nam, B. S. Kim, M. D. Johnson, D.-S. Kong, H. J. Seol, J.-I. Lee, K. M. Joo, Y. Yoon, W.-Y. Park, J. Lee, P. J. Park, and D.-H. Nam (2015). Spatiotemporal Evolution of the Primary Glioblastoma Genome. *Cancer Cell 28*(3), 318–328.

Lacroix, M., D. Abi-Said, D. R. Fourney, Z. L. Gokaslan, W. Shi, F. DeMonte, F. F. Lang, I. E. McCutcheon, S. J. Hassenbusch, E. Holland, K. Hess, C. Michael, D. Miller, and R. Sawaya (2001). A multivariate analysis of 416 patients with glioblastoma multiforme: prognosis, extent of resection, and survival. *Journal of Neurosurgery 95*(2), 190–198.

Law, M., S. Oh, J. S. Babb, E. Wang, M. Inglese, D. Zagzag, E. A. Knopp, and G. Johnson (2006). Low-grade gliomas: Dynamic susceptibility-weighted contrast-enhanced perfusion mr imaging—prediction of patient clinical response. *Radiology 238*(2), 658–667.

Lee, J.-K., J. Wang, J. K. Sa, E. Ladewig, H.-O. Lee, I.-H. Lee, H. J. Kang, D. S. Rosenbloom, P. G. Camara, Z. Liu, P. van Nieuwenhuizen, S. W. Jung, S. W. Choi, J. Kim, A. Chen, K.-T. Kim, S. Shin, Y. J. Seo, J.-M. Oh, Y. J. Shin, D.-S. Kong, H. J. Seol, A. Blumberg, J.-I. Lee, A. Iavarone, W.-Y. Park, R. Rabadan, and D.-H. Nam (2016). Space-time genomic architecture informs precision oncology in glioblastoma. Under revision.

Leong, L. C. H., E. C. Gombos, J. Jagadeesan, and S. M. C. Fook-Chong (2015). MRI Kinetics With Volumetric Analysis in Correlation With Hormonal Receptor Subtypes and Histologic Grade of Invasive Breast Cancers. *AJR Am. J. Roentgenol. 204*(3).

Li, W.-b., K. Tang, Q. Chen, S. Li, X.-g. Qiu, S.-w. Li, and T. Jiang (2012). Mri manifestions correlate with survival of glioblastoma multiforme patients. *Cancer Biology & Medicine 9*(2), 120–123.

Lipman, Y. and I. Daubechies (2011). Conformal Wasserstein Distances: Comparing Surfaces in Polynomial Time. *Advances in Mathematics 227*(3), 1047–1077.

Liu, Q., Y. Liu, W. Li, X. Wang, R. Sawaya, F. F. Lang, W. K. A. Yung, K. Chen, G. N. Fuller, and W. Zhang (2015). Genetic, epigenetic, and molecular landscapes of multifocal and multicentric glioblastoma. *Acta Neuropathologica 130*(4), 587–597.

Macyszyn, L., H. Akbari, J. M. Pisapia, X. Da, M. Attiah, V. Pigrish, Y. Bi, S. Pal, R. V. Davuluri, L. Roccograndi, N. Dahmane, M. Martinez-Lage, G. Biros, R. L. Wolf, M. Bilello, D. M. O'Rourke, and C. Davatzikos (2016). Imaging patterns predict patient survival and molecular subtype in glioblastoma via machine learning techniques. *Neuro-Oncology 18*(3), 417–425.

Mazurowski, M. A., A. Desjardins, and J. M. Malof (2013). Imaging descriptors improve the predictive power of survival models for glioblastoma patients. *Neuro-Oncology*.

Mazurowski, M. A., J. Zhang, K. B. Peters, and H. Hobbs (2014). Computer-extracted mr imaging features are associated with survival in glioblastoma patients. *Journal of Neuro-Oncology 120*(3), 483–488.

Mileyko, Y., S. Mukherjee, and J. Harer (2011). Probability measures on the space of persistence diagrams. *Inverse Problems 27*(12), 124007.

Mohammadi, A. M., J. L. Schroeder, L. Angelov, S. T. Chao, E. S. Murphy, J. S. Yu, G. Neyman, X. Jia, J. H. Suh, G. H. Barnett, and M. A. Vogelbaum (2016, 2016/10/27). Impact of the radiosurgery prescription dose on the local control of small (2 cm or smaller) brain metastases. *Journal of Neurosurgery*, 1–9.

Munkres, J. R. (1984). *Elements of algebraic topology*, Volume 2. Addison-Wesley Reading.

Patel, M. A., J. E. Kim, J. Ruzevick, G. Li, and M. Lim (2014). The future of glioblastoma therapy: Synergism of standard of care and immunotherapy. *Cancers 6*(4), 1953.

Pope, W. B., X. J. Qiao, H. J. Kim, A. Lai, P. Nghiemphu, X. Xue, B. M. Ellingson, D. Schiff, D. Aregawi, S. Cha, V. K. Puduvalli, J. Wu, W.-K. A. Yung, G. S. Young, J. Vredenburgh, D. Barboriak, L. E. Abrey, T. Mikkelsen, R. Jain, N. A. Paleologos, P. Lada, M. Prados, J. Goldin, P. Y. Wen, and T. Cloughesy (2012). Apparent diffusion coefficient histogram analysis stratifies progression-free and overall survival in patients with recurrent gbm treated with bevacizumab: a multi-center study. *Journal of Neuro-Oncology 108*(3), 491–498.

R Core Team (2016). *R: A Language and Environment for Statistical Computing*. Vienna, Austria: R Foundation for Statistical Computing.

Raza, S. M., F. F. Lang, B. B. Aggarwal, G. N. Fuller, D. M. Wildrick, and R. Sawaya (2002). Necrosis and glioblastoma: A friend or a foe? a review and a hypothesis. *Neurosurgery 51*(1).

Rios Velazquez, E., R. Meier, W. D. Dunn, B. Alexander, R. Wiest, S. Bauer, D. A. Gutman, M. Reyes, and H. J. W. L. Aerts (2015). Fully automatic GBM segmentation in the TCGA-GBM dataset: Prognosis and correlation with VASARI features. *Scientific Reports 5*, 16822.

Sargent, D., H. Wieand, D. Haller, R. Gray, J. Benedetti, M. Buyse, R. Labianca, J. Seitz, C. O'Callaghan, G. Francini, A. Grothey, M. O'Connell, P. Catalano, C. Blanke, D. Kerr, E. Green, N. Wolmark, T. Andre, R. Goldberg, and A. De Gramont (2005). Disease-free survival versus overall survival as a primary end point for adjuvant colon cancer studies: Individual patient data from 20,898 patients on 18 randomized trials. *Journal of Clinical Oncology 23*(34), 8664–8670.

Servin, B. and M. Stephens (2007). Imputation-based analysis of association studies: Candidate regions and quantitative traits. *PLoS Genet 3*(7), e114–.

Skrondal, A. and S. Rabe-Hesketh (2009). Prediction in multilevel generalized linear models. *Journal of the Royal Statistical Society: Series A (Statistics in Society) 172*(3), 659–687.

Subramanian, A., P. Tamayo, V. K. Mootha, S. Mukherjee, B. L. Ebert, M. A. Gillette, A. Paulovich, S. L. Pomeroy, T. R. Golub, E. S. Lander, and J. P. Mesirov (2005). Gene

set enrichment analysis: a knowledge-based approach for interpreting genome-wide expression profiles. *Proc Natl Acad Sci U S A 102*(43), 15545–15550.

Talos, I.-F., K. H. Zou, R. Kikinis, and F. A. Jolesz (2007). Multidimensional profiling of cell surface proteins and nuclear markers. *Acad. Radiol. 14*(4), 431–436.

Taylor, J. E. and R. J. Adler (2003). Euler characteristics for gaussian fields on manifolds. *Ann. Probab. 31*(2), 533–563.

Turner, K., Y. Mileyko, S. Mukherjee, and J. Harer (2014). Fréchet means for distributions of persistence diagrams. *Discrete & Computational Geometry 52*(1), 44–70.

Turner, K., S. Mukherjee, and D. M. Boyer (2013). Persistent Homology Transform for Modeling Shapes and Surfaces. *ArXiv e-prints*.

Turner, K., S. Mukherjee, and D. M. Boyer (2014). Persistent homology transform for modeling shapes and surfaces. *Information and Inference 3*(4), 310–344.

Tykocinski, E. S., R. A. Grant, G. S. Kapoor, J. Krejza, L.-E. Bohman, T. A. Gocke, S. Chawla, C. H. Halpern, J. Lopinto, E. R. Melhem, and D. M. O'Rourke (2012). Use of magnetic perfusion-weighted imaging to determine epidermal growth factor receptor variant iii expression in glioblastoma. *Neuro-Oncology 14*(5), 613–623.

Verhaak, R. G. W., K. A. Hoadley, E. Purdom, V. Wang, Y. Qi, M. D. Wilkerson, C. R. Miller, L. Ding, T. Golub, J. P. Mesirov, G. Alexe, M. Lawrence, M. O'Kelly, P. Tamayo, B. A. Weir, S. Gabriel, W. Winckler, S. Gupta, L. Jakkula, H. S. Feiler, J. G. Hodgson, C. D. James, J. N. Sarkaria, C. Brennan, A. Kahn, P. T. Spellman, R. K. Wilson, T. P. Speed, J. W. Gray, M. Meyerson, G. Getz, C. M. Perou, and D. N. Hayes (2010). Integrated genomic analysis identifies clinically relevant subtypes of glioblastoma characterized by abnormalities in pdgfra, idh1, egfr, and nf1. *Cancer Cell 17*(1), 98–110.

Wedeen, V. J., D. L. Rosene, R. Wang, G. Dai, F. Mortazavi, P. Hagmann, J. H. Kaas, and W.-Y. I. Tseng (2012). The geometric structure of the brain fiber pathways. *Science 335*(6076), 1628.

Weller, M., T. Cloughesy, J. R. Perry, and W. Wick (2012). Standards of care for treatment of recurrent glioblastoma—are we there yet? *Neuro-Oncology*.

Zhang, M., S. Zhang, Y. Wen, Y. Wang, Y. Wei, H. Liu, D. Zhang, J. Su, F. Wang, and Y. Zhang (2015). DNA Methylation Patterns Can Estimate Nonequivalent Outcomes of Breast Cancer with the Same Receptor Subtypes. *PLoS One. 1*(10), e0142279.

Zhou, X., P. Carbonetto, and M. Stephens (2013). Polygenic modeling with Bayesian sparse linear mixed models. *PLoS Genet 9*(2), e1003264.